



Detecting thermal anomalies in lahendong geothermal prospect using ASTER TIR and Landsat 8

Mohammad Aftaf Muhajir^a, Kudang Boro Seminar^b, Leopold Oscar Nelwan^b

^a Master of Science in Information Technology for Natural Resources Management, Faculty of Mathematics and Natural Resources, IPB University, IPB Darmaga Campus, Bogor, 16680, Indonesia

^b Department of Mechanical and Biosystem Engineering, Faculty of Agricultural Technology, IPB University, IPB Darmaga Campus, Bogor, 16680, Indonesia

Article Info:

Received: 21 - 04 - 2022

Accepted: 25 - 08 - 2023

Keywords:

ASTER TIR, land surface temperature, landsat 8, geothermal anomalies, surface manifestation

Corresponding Author:

Mohammad Aftaf Muhajir
Master of Science in Information Technology for Natural Resources Management, Faculty of Mathematics and Natural Resources, IPB University;
Phone: +628119822558
Email:
mohammad_aftaf@apps.ipb.ac.id

Abstract. *In this study, we set out to find unusual patterns in specific areas using data from Landsat 8 and ASTER satellites, including Thermal Infrared Sensor (TIRS) data. We used various techniques like georeferencing, radiometric calibration, and atmospheric correction to examine land surface temperatures (LST) during the day and night. We focused on four types of natural land cover: water bodies, vegetation, built-up areas, and barren land. Interestingly, we noticed that water bodies had cooler temperatures during the day but got warmer at night, while vegetation was cooler at night and warmer during the day. To accurately spot areas with higher temperature anomalies, while filtering out colder spots due to sunlight, we overlaid daytime and nighttime LST data based on land cover types. Additionally, we used thematic maps from satellite images to pinpoint village areas. To double-check the anomalies we observed, we compared our findings with geological maps. Through this approach, we successfully identified nine distinct regions where temperatures were 3 to 6 degrees Kelvin higher than the normal background temperature.*

How to cite (CSE Style 8th Edition):

Muhajir MA, Seminar KB, Nelwan LO. 2023. Detecting thermal anomalies in lahendong geothermal prospect using ASTER TIR and Landsat 8. *JPSL* 13(3): 494–503. <http://dx.doi.org/10.29244/jpsl.13.3.494-503>.

INTRODUCTION

The sustainability of various activities within the community, which is also influenced by the national industrial sector, depends on the supply of electricity. This has resulted in an increasing need for a reliable supply of electrical energy. Therefore, the electricity sector plays a strategic role in determining efforts to improve community welfare and encourage the national economy to run. In accordance with Act No. 30 of 2007 on Energy, maintaining the security and sustainability of domestic energy supply requires cooperation and synergistic efforts from the government, private sector, and public. The lack of actions to anticipate and ensure the sustainability of the energy supply from the start will result in more costly consequences in the future.

To address the pressing issues of our energy supply and combat the environmental challenges associated with global warming, the utilization and advancement of renewable energy resources have become more crucial than ever. The government, as laid out in Presidential Regulation No. 5 of 2006 on National Energy Policy, has taken steps to create a national energy management plan covering the period from 2006 to 2025.

According to this plan, the goal is for 17% of our nation's energy to come from renewable sources, highlighting the pivotal role that renewable energy will play in our future. Indonesia is fortunate to possess a diverse array of new and renewable energy sources, including geothermal, hydropower, biomass, solar energy, and marine energy. Indonesia's unique geographic location, nestled amidst the dynamic tectonic plates of Indo-Australian, Pacific, Philippines, and Eurasian, positions it as one of the world's most geologically active regions. This favorable positioning grants Indonesia an abundance of geothermal energy resources, scattered across 285 locations along the volcanic arc, boasting an impressive potential of 29,215 Gigawatt electrical (GWe).

Geothermal is a source of heat energy contained in hot water, water vapor, and rock along with other minerals and other gases that are genetically inseparable in a geothermal system and for its utilization required mining process (Law No. 21 of 2014). Geothermal systems are typically found in areas where the Earth's crust contains a significant amount of heat. This elevated heat is linked to the presence of young igneous or hot rocks located deeper within the Earth's crust (DiPippio 2005). The surplus geothermal heat that becomes evident at the Earth's surface is a result of the movement of groundwater, creating what is known as a hydrothermal system. Surface water travels to great depths, where it gets heated, and then it rises back to the surface through underground "pipe systems" connected to nearby fractures or other permeable rock formations. When these heated waters breach the surface, they can give rise to distinct geothermal phenomena like hot springs, fumaroles, geysers, and mud pots.

Thermal Infrared remote sensing data proves valuable in mapping and quantifying temperature variations associated with surface geothermal features like hot springs, geysers, fumaroles, and heated ground. This approach can economize geothermal exploration across extensive areas, facilitating the detection of potential sites for further investigation through on-site surveys (Hodder 1970; Lee 1978; Mongillo 1994; Haselwimmer and Prakash 2011). Moreover, thermal infrared remote sensing has found applications in documenting and monitoring the long-term temperature characteristics of developed and safeguarded geothermal systems (Mongillo 1994; Seielstad and Queen 2009).

Remote sensing technology offers a way to understand the characteristics of objects or areas on Earth's surface without the need for direct physical examination. In this study, our aim is to find regions with geothermal anomalies using data from remote sensing, specifically Landsat 8 and the Advanced Spaceborne Thermal Emission and Reflection Radiometer (ASTER) Satellite images. These images come with a Thermal Infrared Sensor (TIRS) that helps us spot differences in surface temperature anomalies across the Earth's surface.

MATERIALS AND METHOD

Study Area

This study was conducted between March and December 2020. Lahendong, North Sulawesi, was chosen as the research location for data collection, while data processing was conducted at the MIT for NRM (Master of Science in Information Technology for Natural Resources Management) Computer Lab, Biotrop, Bogor, West Java. Lahendong is a geothermal area in Tomohon, North Sulawesi, which is about 30 kilometers south of Manado, the provincial capital. It's in a spot on Sulawesi Island shaped by geological processes, and the region where Lahendong is situated is part of the Tondano Depression, which is like a valley that stretches about 20 kilometers from north to south and opens to the west. In this depression, Pangolombian rim is found as a significant feature in the Lahendong geothermal system (Koestono et al. 2010).

Material

Primary Data

For our study, we relied on data from two satellite sources: Landsat 8, which has a TIRS, and ASTER sensor on the Terra Satellite. We chose the year 2018 as our focus because, according to satellite records from

Landsat 8 and ASTER TIR spanning 2018 to 2020, it had the least cloud cover during the same season. It's worth noting that the temperature data we collected was from clear scenes, without any cloud interference. To address the impact of sunlight on the Earth's surface, we employed land surface temperature (LST) data from remote sensing images, considering both day and night conditions. These images were carefully adjusted for radiance and underwent correction for any geometric distortions, referred to as "level 1T." In particular, we made use of ASTER TIR bands for nighttime data in 2018 and Landsat 8 TIRS daytime data from the same year, as detailed in Table 1. This method allowed us to effectively spot areas with unusual temperature patterns.

Table 1 Landsat 8 and ASTER TIR acquisition date

Satellite	Acquisition Date	Path	Row
Landsat 8	9/2/2018	112	59
ASTER TIR	12/3/2018	220	185

Secondary Data

We relied on a detailed topographic map, generously provided by the *Badan Informasi Geospasial (BIG)*, with a scale of 1:50,000. This map aided us in identifying key features like roads, rivers, and settlements. To determine the ground elevation in the area, we consulted the Digital Elevation Model Nasional (DEMNAS), also made available by BIG. Additionally, we referred to a geological map by Siahhaan et al. (2005) and Utami et al. (2004) to gain insights into the geological characteristics of the study area.

Methods

Our research journey consisted of several important stages, each contributing significantly to our findings. Initially, we focused on improving the quality of our remote sensing data by addressing factors like atmospheric, radiometric, and geometric distortions, ensuring the reliability of our information. Following this, we calculated LST and emissivity for both Landsat and ASTER datasets using the Planck function inversion method, following the procedures outlined by Stathopoulou and Cartalis (2007). We also carefully selected the most suitable ASTER band for LST retrieval, settling on bands 13 and 14, with band 14 being our choice for ASTER data analysis. Subsequently, we conducted a statistical analysis, overlaying daytime and nighttime LST images to devise a method for detecting geothermal anomalies. This involved determining a suitable threshold to distinguish between regular temperature values and anomalies, a crucial step in our geothermal investigation. Lastly, our research involved a thorough examination of geothermal anomalies using preprocessed medium-resolution satellite imagery, with these anomalies being a key focal point of our study.

Image Preprocessing

The data quality from specific Landsat 8 OLI bands, namely the red (band 4), near-infrared (band 5), and TIRS thermal infrared band 10 (with wavelengths ranging from 10.60 to 11.19 μm), was significantly improved through rigorous radiometric calibration and atmospheric correction processes. To ensure precise correction for variations related to terrain, we relied on orthorectified images provided by the United States Geological Survey (USGS). Radiometric calibration, a vital component of our methodology, was systematically applied to convert the recorded Digital Number (DN) values from the remote sensors into atmospheric radiance images, following the prescribed Equation 1. Notably, the USGS in 2015 furnished us with the requisite radiance multiplicative scaling factor (ML) and radiance additive scaling factor (AL), enabling us to compute spectral radiance in accordance with established procedures.

$$L\lambda = MLQ_{cal} + AL$$

In this context, $L\lambda$ represents the spectral radiance at the top of the atmosphere (TOA), measured in units of $W/m^2/sr \cdot \mu m^{-1}$, while ML stands for a band-specific multiplicative scaling factor derived from the metadata, typically labeled as $RADIANCE_MULT_BAND_x$, with 'x' indicating the specific band number. AL, similarly band-specific, represents an additive scaling factor, sourced from the metadata as $RADIANCE_ADD_BAND_x$. Lastly, Q_{cal} denotes the pixel value in our data after quantization and calibration, expressed as DN. To convert the spectral radiance data of the TIRS bands into brightness temperature, we utilize thermal constants provided within the metadata file, guided by Equation:

$$T = K2 / (\ln (K1 / L\lambda + 1))$$

T represents the brightness temperature as observed by the satellite, measured in Kelvin (K). $L\lambda$ stands for the spectral radiance at the TOA, given in units of $W/m^2/sr \cdot \mu m^{-1}$. K1 is a thermal conversion constant specific to the band and can be found in the metadata under $K1_CONSTANT_BAND_x$, with 'x' indicating the band number, which can be either 10 or 11. Similarly, K2 is another band-specific thermal conversion constant sourced from the metadata as $K2_CONSTANT_BAND_x$, again with 'x' representing the band number, which can be either 10 or 11. These constants are essential for converting spectral radiance into brightness temperature.

The process of calculating ASTER surface temperatures begins with the conversion of Digital Numbers (DNs) to radiance. For this purpose, the equation can be expressed as follows:

$$L\lambda = (DN - 1) \times UCC$$

$L\lambda$ stands for spectral radiance, which essentially measures the amount of light emitted across various wavelengths. DN, on the other hand, represents the digital values obtained from the thermal infrared (TIR) band readings. The parameter UCC is a significant unit conversion coefficient ($0.005225 W/m^2/sr \cdot \mu m^{-1}$) used to translate these readings into meaningful units. For precise details on the coefficients (K1 and K2) specific to the TIR bands of the ASTER instrument, you can refer to Table 2. The resulting temperature, measured in Kelvin, is determined by applying:

$$T = K2 / (\ln (K1 / L\lambda + 1))$$

Table 2 K1 and K2 coefficients of the TIR bands of the ASTER instrument

Band	K1 ($W \cdot m^2 \cdot sr^{-1} \cdot \mu m^{-1}$)	K2 ($W \cdot m^2 \cdot sr^{-1} \cdot \mu m^{-1}$)
Band 10	3,047.47	1,736.18
Band 11	2,480.93	1,666.21
Band 12	1,930.80	1,584.72
Band 13	865.65	1,349.82
Band 14	649.60	1,274.49

Landsat 8 OLI Emissivity and LST Calculation

For the OLI images, we applied radiance-to-reflectance conversions and conducted atmospheric corrections using the DOS1 method to enhance our understanding of the Earth's surface. We utilized the normalized difference vegetation index threshold method (NDVITHM) to estimate Land Surface Emissivity (LSE) and LST. Interestingly, there was no need for atmospheric correction when we worked with the TIRS band. Initially, the TIRS bands provided data at a 100 meter resolution, but since 2010, the USGS resampled them to a finer 30 meter resolution using cubic convolution to match the spectral bands of the OLI Sensor.

Various methods are available for estimating LSE and LST using remote sensing data. In this research, the NDVITHM approach, which has undergone further refinement and development by prior researchers, including Sobrino et al. (2001) and Valor and Caselles (1996), was employed. To calculate LSE, the statistical

relationship between the Normalized Difference Vegetation Index (NDVI) and emissivity across the TIR spectral bands within the NDVITHM framework was utilized. Specifically, Band 10 from Landsat 8 was chosen due to reported calibration instability in Band 11, as noted by Barsi et al. (2014). Equation below presents the mathematical expression that facilitates the determination of LSE, taking into account NDVI, vegetation characteristics, and soil emissivity.:

$$\varepsilon = 0.004 P_v + 0.986$$

Here, ε represents emissivity, and P_v denotes the proportion of vegetation. P_v is derived from the NDVI value and subsequently inserted into:

$$P_v = (NDVI - NDVI_{min} / NDVI_{max} - NDVI_{min})^2$$

The calculation of LST was accomplished using the Planck inversion function, as introduced by Stathopoulou and Cartalis (2007):

$$LST = BT/1 + \lambda \times (BT/p) \times Ln(\varepsilon)$$

Where λ is wavelength of emitted radiance, ε denotes LSE and p is equal to 14,380.

ASTER Emissivity and LST Calculation

The calculation of Land Surface Emissivity (LSE) in this study was based on the NDVI approach, a method widely utilized for estimating LSE across different sensors using visible and near-infrared (VNIR) data. To determine NDVI this equation was used in this study:

$$NDVI = \frac{NIR - R}{NIR + R}$$

NIR denotes the reflectance in the near-infrared band, and R signifies the reflectance in the red band captured by the ASTER sensor. The algorithm developed by Jiménez-Muñoz and Sobrino (2009) was employed in this study to estimate Land Surface Emissivity (LSE) based on NDVI. This choice was made due to its rigorous validation with in situ data for ASTER TIR bands 10 to 14, as elaborated in Equations below:

$$\varepsilon_{10} = 0.946 + 0.044P_v$$

$$\varepsilon_{11} = 0.949 + 0.041P_v$$

$$\varepsilon_{12} = 0.941 + 0.049P_v$$

$$\varepsilon_{13} = 0.968 + 0.022P_v$$

$$\varepsilon_{14} = 0.970 + 0.020P_v$$

ε represents thermal infrared emissivity in individual channels, while P_v signifies the fraction of vegetation, occasionally known as fractional vegetation cover. The calculation of the vegetation fraction was derived from the computation of NDVI. $NDVI_v$ corresponds to the NDVI value attributed to vegetation, whereas $NDVI_s$ represents the NDVI value assigned to soil. Specifically, $NDVI_v$ was set at 0.7, and $NDVI_s$ was established as 0.05. These particular values were determined by analyzing the NDVI histogram, following the approach outlined by Xiong et al. (2019).

$$P_v = (NDVI - NDVI_s / NDVI_v - NDVI_s)^2$$

The Planck function served as a fundamental tool in calculating thermal radiation intensity. It quantifies the thermal electromagnetic wave emissions from an object, assuming it behaves as a blackbody in equilibrium at a known temperature. With knowledge of the LSE in a specific area, we can estimate the LST by inverting the Planck function. This inversion process relies on the assumption that the land surface can be considered a black body, characterized by an emissivity of 1. The use of the Planck function validates the correction of emissivity in brightness temperature calculations. In this study, the Planck function played a central role in estimating LST. The formula for computing emissivity-corrected land surface temperature is made available through the Planck inversion function, introduced by Stathopoulou and Cartalis in 2007. Additionally, Table 3 offers information on the effective wavelengths of the TIR bands.

Table 3 Effective wavelengths (λ) of the TIR channels of the ASTER instrument

Band	Effective wavelength (λ) in μm
Band 10	8.287
Band 11	8.685
Band 12	9.079
Band 13	10.659
Band 14	11.289

Determining Geothermal Anomaly

Utilizing geological mapping, geothermal anomalies within the LSTs map were confirmed. The study identified regions with LSTs approximately 3–6 K higher than the background temperatures. Previous research conducted by Siahaan et al. (2005) extensively documented the geological characteristics of the Lahendong geothermal field, encompassing altered terrains and thermal manifestations. These thermal manifestations primarily cluster along the western and northern shores of Linau Lake, spanning across Leilem, Lahendong, and Kasuratan Villages. They predominantly belong to the steam-heated type and are often aligned with NE-SW trending faults. Notably, neutral pH water discharges were not identified within the Lahendong area.

These thermal manifestations manifest in various forms, including altered and steaming ground, acidic-sulfate hot springs, mud pots, mud pools (with or without mud volcanoes), and sulfide gas emissions. Common minerals found in these altered terrains include kaolin, residual silica, sulfur, very fine-grained pyrite, aluminous salts, and iron oxide. The most vigorous thermal activity is concentrated in the Linau area, home to fumaroles with temperatures as high as 106 °C. The study area also encompasses the hottest steaming ground (T = 60–98 °C at a depth of 45 cm) and the most scorching acid-sulfate springs (T = 80–90 °C, pH = 2–4).

According to data provided by the Ministry of Energy and Mineral Resources in 2017, three specific occurrences were designated as fumaroles. These fumaroles were situated in the vicinity of Lake Linau, Lailem Village, and Lahendong (Table 4). Brehme et al. (2019) compared fault locations with hot springs. On the map, hot springs are given the symbol M which indicates surface manifestation. Some of the identified surface manifestations were M1, M2, M3, M4, M10, M11, M13, M15, M16, and M17. The fault location characteristics of hot springs in Lahendong indicate that hot springs are present under certain types of conditions, for example, at fault tips, intersections, and fault lines. Unclear hot springs were assumed to be hidden faults.

Table 4 Surface manifestation

Location	Types	X	Y	Elevation	Temp °C	(pH)
Linau	Fumarole	124 ⁰ 49' 18.81'' E	1 ⁰ 16' 8.65'' N	812	92	2
Lailem	Fumarole	124 ⁰ 49' 11.21'' E	1 ⁰ 16' 4.39'' N	779	90	2
Lahendong	Fumarole, Mudpool	124 ⁰ 48' 45.32'' E	1 ⁰ 16' 26.84'' N	700	89	2

Source: ESDM (2017)

RESULTS AND DISCUSSION

Daytime LST extracted by Landsat 8

For the TIR band of the Landsat 8 TIRS sensor, K1 and K2 were constants obtained from the data's metadata file. NDVI min and NDVI max were determined through calculations involving NDVI values. Land surface emissivity (ϵ) was then computed by multiplying the proportion of vegetation (P_v) by 0.004 and then adding 0.986. Then the land surface temperatures (Figure 1) were calculated by utilizing the Planck inversion function introduced by Stathopoulou and Cartalis (2007), utilizing the coefficients provided in Table 2. Throughout daylight hours, surface temperatures ranged from 293.76 K to 304.43 K, with an average of 297.48 K and a standard deviation of 1.63 (Figure 2).

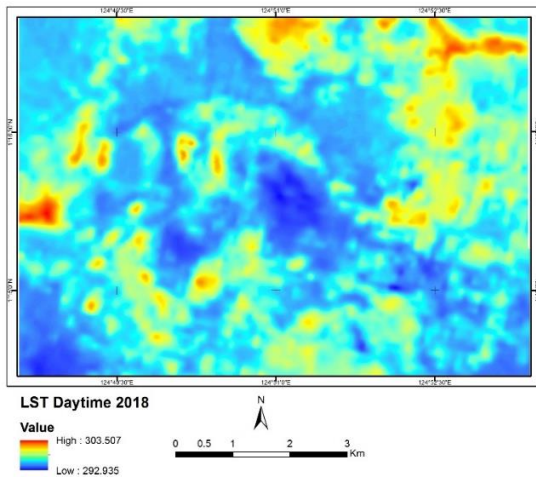


Figure 1 Landsat 8 daytime land surface temperature band 10

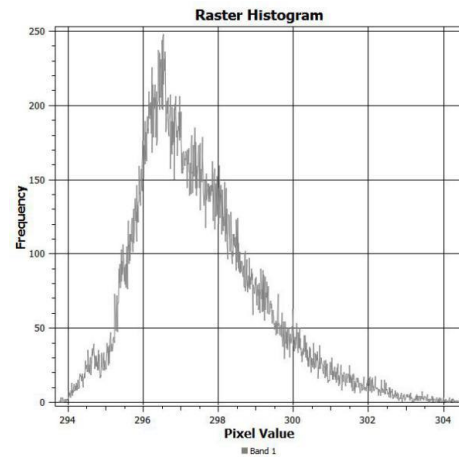


Figure 2 Daytime histogram of land surface temperature extracted by Landsat 8 Band 10

Nighttime LST extracted by ASTER TIR

This study aimed to estimate LST using ASTER TIR data. The Planck function inversion technique was employed for this purpose, and it allowed us to derive the Emissivity (ϵ) values using the Jiménez-Muñoz et al. (2006) algorithm.

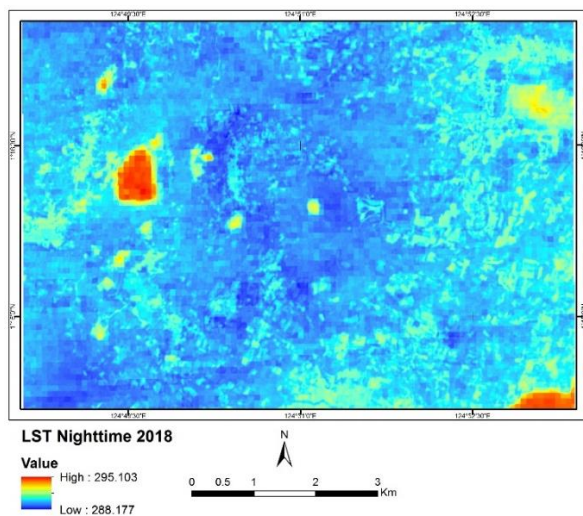


Figure 3 ASTER TIR nighttime land surface temperature band 14

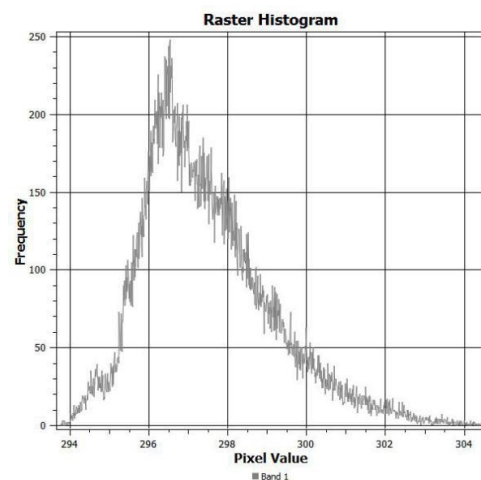


Figure 4 Nighttime histogram of land surface temperature extracted by ASTER TIR Band 14

To highlight the vegetation characteristics, the study involved the calculation of the NDVI, a widely-used indicator of vegetation health. Importantly, NDVI_v represented areas abundant in vegetation with a fixed value of 0.7, while NDVIs represented regions dominated by soil and maintained a value of 0.05. These specific values were derived from the NDVI histogram following the methodology outlined by Xiong et al. (2019). The study's primary focus revolved around the inversion of LST during nighttime in the year 2018, and the resulting outcomes are presented in Figure 3. This depiction provides a comprehensive view of temperature distribution, spanning from 288.18 K to 295.10 K, with an average of 290.05 K and a standard deviation of 0.79, as visually represented in Figure 4. These findings significantly contribute to our understanding of thermal conditions within the study area during the night.

Geothermal Anomalies in Lahendong Area

Within urban and suburban settings, encompassing diverse land cover types such as vegetation, barren land, built-up areas, and water, an extensive analysis of temperature distributions was conducted. Table 5 and Table 6 offer insights into these temperature patterns. In daylight hours, water bodies primarily exhibited temperature ranges from 293.42 K to 300.46 K, categorizing them as relatively cooler anomalies. During the night, water bodies displayed temperature ranges spanning 289.29 K to 295.10 K, marking them as relatively warmer anomalies. Conversely, vegetated regions exhibited distinct diurnal temperature profiles, featuring higher temperature anomalies, ranging from 292.94 K to 301.45 K during the day. In contrast, nighttime temperatures in vegetated areas primarily ranged from 288.209 K to 293.798 K, signifying cooler nighttime conditions and warmer daytime temperatures. These findings underscore the diurnal temperature fluctuations within vegetated landscapes.

Table 5 Day time temperature for different land cover types.

Land cover types	LST at day				
	Min	Max	Range	Mean	Stdev
Barren Land	293.00	302.88	9.88	297.12	1.36
Vegetation	292.94	301.45	8.52	295.51	0.89
Built-up Area	293.86	303.51	9.65	298.74	1.75
Water	293.42	300.46	7.04	295.43	0.98

Table 6 Nighttime temperature for different land cover types

Land cover types	LST at night				
	Min	Max	Range	Mean	Stdev
Barren Land	288.20	294.53	6.33	290.10	0.67
Vegetation	288.21	293.80	5.59	289.73	0.43
Built-up Area	288.18	294.60	6.43	290.44	0.69
Water	289.30	295.10	5.80	293.68	1.41

To precisely locate the areas with elevated temperature anomalies within the geothermal anomaly zone, we conducted a comprehensive analysis of both daytime and nighttime LSTs. This dual approach effectively filtered out the temperature anomalies induced by solar radiation on various land covers. Additionally, we applied Geographical Information System (GIS) analysis to identify any misleading anomalies within urban and village areas. This involved the use of thematic maps created from online imagery, such as digitized representations of built-up areas, to accurately determine urban and village regions. Furthermore, a geological map was instrumental in providing context for these geothermal areas. Throughout our study, we successfully identified anomalous areas where LSTs were consistently 3–6 K higher than the surrounding background temperatures. Based on Brehme et al. (2019) and Siahaan et al. (2005), nine geothermal anomalous identified

as surface manifestation areas including fumaroles (M2, M11 and M17), springs, and other manifestation on Mean LST, including M1, M2, M3, M4, M11, M13, M15, M16, and M17 (Figure 5).

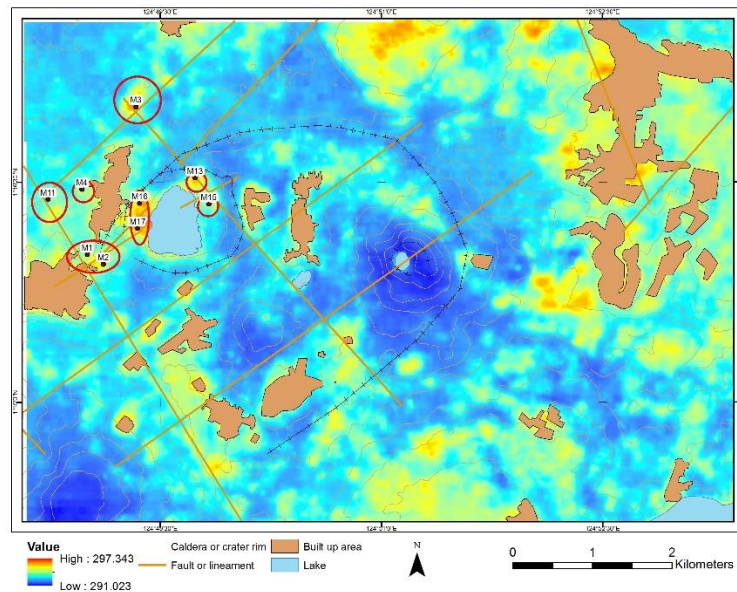


Figure 5 Highlighted areas with unusual LST, delineated by red and irregular boundaries

CONCLUSION

In summary, the utilization of GIS analysis proves effective in the detection and exclusion of false anomalies associated with urban and village areas. Furthermore, the integration of thematic and geological maps greatly enhances our ability to interpret geothermal anomalies with precision. The identification of geothermal regions is based on a thorough analysis, merging geothermal mechanisms with a comprehensive regional geological investigation. These findings robustly demonstrate a close association between the distribution of geothermal areas and the presence of faulted structures within our study area.

The combined analysis of daytime and nighttime LSTs through superimposition effectively mitigates the impact of solar radiation-induced cooler thermal anomalies associated with land cover. This methodology has demonstrated successful application in geothermal exploration within the geothermal anomaly zone of Lahendong, North Sulawesi. The outcomes affirm that the integration of daytime and nighttime TIR remote sensing represents a highly efficient approach for geothermal detection, offering the additional advantage of cost reduction in geothermal exploration efforts. Thus, nine geothermal anomalies areas were successfully extracted.

REFERENCES

- [ESDM] Kementerian Energi dan Sumber Daya Mineral. 2017. *Potensi Panas Bumi Indonesia Jilid 1*. Jakarta: Direktorat Panas Bumi, ESDM.
- [PRI] Pemerintah Republik Indonesia. 2006. Peraturan Presiden Nomor 5 Tahun 2006 tentang Kebijakan Energi Nasional. Jakarta: Sekretariat Negara Republik Indonesia.
- [PRI] Pemerintah Republik Indonesia. 2007. Undang-undang Nomor 30 Tahun 2007 tentang Energi. Jakarta: Sekretariat Negara Republik Indonesia.
- [PRI] Pemerintah Republik Indonesia. 2014. Undang-Undang Republik Indonesia Nomor 21 Tahun 2014 Tentang Panas Bumi. Jakarta: Sekretariat Negara Republik Indonesia.
- [USGS] United States Geological Survey. 2015. *Landsat 8 (L8) Data Users, Handbook Version 1.0*. Sioux Falls. South Dakota: Earth Resources Observation and Science (EROS).

- Barsi JA, Schott JR, Hook SJ, Raqueno NG, Markham BL, Radocinski RG. 2014. Landsat-8 thermal infrared sensor (TIRS) vicarious radiometric calibration. *Remote Sensing*. 6(11):11607–11626.
- Brehme M, Giese R, Suherlina L, Kamah Y. 2019. Geothermal sweetspots identified in a volcanic lake integrating bathymetry and fluid chemistry. *Scientific Reports*. 9(1):1–10.
- DiPippo R. 2005. *Geothermal Power Plants: Principles, Applications and Case Studies*. Oxford: Elsevier Advanced Technology.
- Haselwimmer C, Prakash A. 2013. Thermal infrared remote sensing of geothermal systems. In: *Thermal Infrared Remote Sensin*. Dordrecht: Springer. p 453–473.
- Hodder DT. 1970. Application of remote sensing to geothermal prospecting. *Geothermics*. 2:368–380.
- Jiménez-Muñoz JC, Sobrino JA. 2009. A single-channel algorithm for land-surface temperature retrieval from ASTER data. *IEEE Geoscience and Remote Sensing Letters*. 7(1):176–179.
- Jiménez-Muñoz JC, Sobrino JA, Gillespie A, Sabol D, Gustafson WT. 2006. Improved land surface emissivities over agricultural areas using ASTER NDVI. *Remote Sensing of Environment*. 103(4):474–487.
- Koestono H, Siahaan EE, Silaban M, Franzson H. 2010. Geothermal model of the Lahendong geothermal field, Indonesia. Proceedings world geothermal congress; 2010 Apr 25–29; Bali, Indonesia. Bali: Proceedings World Geothermal Congress.
- Lee K. 1978. Analysis of thermal infrared imagery of the Black Rock Desert geothermal area. *Q Colo Sch Mines (United States)*. 73(3):31–43.
- Mongillo MA. 1994. Aerial thermal infrared mapping of the Waimangu-Waiotapu geothermal region, New Zealand. *Geothermics*. 23(5-6):511–526.
- Seielstad C, Queen L. 2009. Thermal remote monitoring of the Norris Geyser Basin, Yellowstone National Park. *Final Report for the National Park Service Cooperative Ecosystem Studies Unit*. Agreement (H1200040001), 38.
- Siahaan EE, Soemarinda S, Fauzi A, Silitonga T, Azimudin T, Raharjo IB. 2005. Tectonism and volcanism study in the Minahasa compartment of the north arm of Sulawesi related to Lahendong geothermal field, Indonesia. Proceedings World Geothermal Congress; 2005 Apr 24–29, Antalya, Turkey. Antalya: Proceedings World Geothermal Congress.
- Sobrino JA, Raissouni N, Li ZL. 2001. A comparative study of land surface emissivity retrieval from NOAA data. *Remote Sensing of Environment*. 75(2):256–266.
- Stathopoulou M, Cartalis C. 2007. Daytime urban heat islands from Landsat ETM+ and corine land cover data: an application to major cities in Greece. *Solar Energy*. 81(3):358–368.
- Utami P, Siahaan EE, Azimudin T, Browne PRL, Simmons SF. 2004. Overview of the Lahendong geothermal field, North Sulawesi, Indonesia: a progress report. Proceedings of the 26th NZ Geothermal Workshop; 2004 December 6–9; Taupo, New Zealand. Taupo: Geological Society of New Zealand.
- Valor E, Caselles V. 1996. Mapping land surface emissivity from NDVI: application to European, African, and South American areas. *Remote sensing of Environment*. 57(3):167–184.
- Xiong Y, He J, Ma N, Ren X, Liu C. 2019. Land surface temperature retrieval based on thermal infrared remotely sensed data of Aster. *IOP Conference Series: Earth and Environmental Science*. 300(022027): 1–4.